Volume 1 | Number 1 | Jan 2013 | Pages 1–100

Journal of
Materials Chemistry A

Materials for energy and sustainability
www.rsc.org/materialsA

Li⁺

ROYAL SOCIETY
OF CHEMISTRY

ROYAL SOCIETY
OF CHEMISTRY

www.rsc.org/materialsA

Iron (II) molybdate (FeMoO$_4$) nanorods as high-performance anode of lithium ion battery: structural and chemical evolutions upon cycling†

Zhenyu Zhang‡[a], Wenyue Li‡[b], Tsz-Wai Ng[a], Wenpei Kang[a], Chun-Sing Lee[a], and Wenjun Zhang*[a]

[a]Center of Super-Diamond and Advanced Films (COSDAF), Department of Physics and Materials Science, City University of Hong Kong, Hong Kong

[b]Functional Thin Films Research Centre, Shenzhen Institute of Advanced Technology, Chinese Academy of Sciences, Shenzhen 518055, P. R. China

E-mail: apwjzh@cityu.edu.hk

†Electronic supplementary information (ESI) available.

‡These authors contributed equally to this work.

Keywords: Iron molybdate, lithium ion battery anode, structural evolution, phase transformation

Abstract: FeMoO$_4$ nanorods were synthesized by a one-step solvothermal method and demonstrated to have attractive performance as an anode material in lithium ion batteries (LIBs). The specific capacity of the electrode exhibited an initial fading in the first 50 cycles and subsequently recovered to 1265 mAh g^{-1} at about 500th cycle at a rate of 1C, after that, the capacity maintained stably around 1110 mAh g^{-1} till 1000th cycle. Based on comprehensive analysis of the structural and chemical evolutions at each stage of capacity variation, we illustrated that the FeMoO$_4$ nanorods were converted to Fe$_2$O$_3$/MoO$_3$ mixture since the first cycle and they experienced gradual structural variation of grain refinement and amorphization with morphology transformed from nanorod to nanosheets upon cycling. Such changes in chemical composition and microstructure of nanorods led to larger effective surface area, improved electrochemical reaction kinetics, and capacity retention capability. As similar

tendency of the specific capacity upon cycling has been widely observed for metal oxide anodes, studies on structural and chemical evolutions of electrode materials during the whole cyclic life will be helpful for understanding their electrochemical reaction mechanism and provide guidance to material design and structural optimization of electrodes.

Introduction

To meet the requirements of high energy and power densities, and long life span of lithium ion batteries (LIBs), exploiting new anode materials with high theoretical capacity and optimal micro- or nano-scale structures have been an important research topic. Due to the higher reversible capacities over the commercially used graphite, ternary metal oxides (TMOs) have attracted extensive research interest as alternative anode materials for LIBs.[1-3] Molybdenum-containing TMOs are an important family for anode application because of the high oxidation state of molybdenum.[4] For instance, $CuMoO_4$,[5] $MnMoO_4$,[6] $NiMoO_4$,[7] $CoMoO_4$[8] have been demonstrated to be promising electrode materials for LIBs. However, as an important member of metal molybdates, $FeMoO_4$ has only been studied for the electrochemical applications, such as electrode of oxygen evolution,[9] supercapacitor,[10,11] hydrodesulfurization catalysis,[12] and cathode material of LIBs.[5] Although $FeMoO_4$ has a high theoretical capacity of 992.3 mAh g^{-1} due to the high valences of Fe (+3) and Mo (+6), there have been few investigations on $FeMoO_4$ as anode material of LIBs up to now. Only very recently, Ju et al. reported that $FeMoO_4$ nanocubes could be used as an efficient and reversible lithium storage anode material which exhibits 926 mAh g^{-1} after 80 cycles at a current density of 100 mA g^{-1} ($\sim$0.1C, 1C=992.3 mA g^{-1}) and remarkable rate performance, indicating a good prospect of $FeMoO_4$ for LIB application.[13]

It has been widely accepted that the capacitance of anode materials upon cycling is largely determined by their chemical and structural stabilities during charge/discharge

processes.[14,15] For the anode materials in LIBs such as C, Si, and Sn, it has been usually found that the specific capacity decreased monoclinally with the cycling process due to the mechanical degradation and chemical composition variation by the repeated volume change. However, for TMO anode materials, an increase of the capacity was in general observed after an initial capacity fading, which was illustrated by the activation process of electrode materials.[16-22] For instance, vesiculation was observed in γ-Fe_2O_3@C/MWNT composite[23] which resulted in increased active surface area; Co_3O_4 hollow spheres[24] were shown to transform to mesoporous amorphous nanospheres consisting of enlarged pore size/space and flower-like nanosheets during the electrode activation, which delivered increased capacities along with cycles. These results suggest that, in contrast to the conventional electrode materials, certain structure and chemical composition variations of TMO electrode are beneficial to the improvement of electrochemical performance. Therefore, further investigation on the evolutions of electrode materials during the whole life of batteries is required to understand the electrochemical reaction mechanism and improve the battery performances of TMOs.

In this work, we synthesized $FeMoO_4$ nanorods by a one-step solvothermal method, and demonstrated that they exhibited high capacity and long-term cycling stability as an anode material for LIBs. At a current density of 1C, the battery capacity experienced a fast drop to ~400 mAh g^{-1} in the first ~50 cycles, then it gradually raised up to ~1200 mAh g^{-1} by the ~500th cycle, and maintained at 1100 mAh g^{-1} till 1000th cycle. In order to understand the electrochemical characteristics during long-term cycling, the anode materials at several critical stages were carefully analyzed by employing transmission electron microscopy (TEM), Raman spectra, X-ray photoelectron spectroscopy (XPS) and electrochemical analysis. Based on that, the relationship of the structural/chemical composition evolutions of $FeMoO_4$ nanorod anodes during cycling with the electrode performance was demonstrated.

Experimental Section

Synthesis: The $FeMoO_4$ nanorods are synthesized by one-step solvothermal method. Typically, a solution of 0.08 M $FeCl_2 \cdot 4H_2O$ in triethylene glycol (TEG) was dropwise added into the solution of 0.08 M $Na_2MoO_4 \cdot 2H_2O$ in aqueous while magnetic stirring. The red brown mixed solution was then transferred into a Teflon-lined stainless steel autoclave and maintained at 120 ºC for 24 h in electrical oven. After naturally cooled to room temperature, the precipitate was collected by centrifugation, washed several times with deionized water and ethanol, and vacuum dried at 60°C for 12 h.

Characterization: The product was first characterized by using SEM (Philips XL30 FEG), TEM (Philips FEG CM200, operating at 200 kV), and powder XRD (Philips X'Pert) using CuK_α radiation (λ = 0.15418 nm) with a scanning step of 0.05 (°) s^{-1}. XPS analysis was performed in a VG ESCALAB 220i-XL UHV surface analysis system with a monochromatic Al K_α X-ray source (1486.6 eV). Raman spectra were measured using a Renishaw 2000 Raman microscope with a laser wavelength of 633 nm. The nitrogen adsorption-desorption isotherms of the $FeMoO_4$ nanorods were conducted by Quantachrome NovaWin Nova Station A, from which the specific surface area and pore size distribution curves by the Barrett-Joyner-Halenda (BJH) method of the samples were obtained.

Electrochemical tests: The anodes of LIB were made by mixing active materials ($FeMoO_4$ nanorods), conductivity agent (carbon black) and binder (polyvinylidene fluoride) in a weight ratio of 80:10:10, and coating the mixture on a copper foil with a total weight loading of 1.2 ± 0.3 mg cm^{-2} was vacuum-dried at 60 ºC for 12 h. Coin cells (CR2032) were fabricated with lithium metal as the counter electrode, Celgard 2400 as the separator, and $LiPF_6$ (1M) in ethylene carbonate/dimethyl carbonate (EC/DMC, 1:1 vol %) as the electrolyte, which were assembled in an Ar-filled glovebox (MBRAUN) followed by 24 h aging treatment before test. CV measurement was carried out at a scan rate of 0.1 mV s^{-1} within the range of 0.01-3.0 V

with an electrochemical workstation (CHI 600D). The EIS was recorded by the ZAHNER-elektrik IM 6 electrochemical system over a frequency range 100 KHz to 10 mHz. The charge-discharge measurements of cells were carried out within a fixed voltage window of 0.01-3.0 V by using a battery test system (MACCOR 4000) at room temperature. At different points during the battery test, the cells were stopped and disassembled and the working electrodes were washed using deionized water, ethanol and acetone, separately. The corresponding cycling curves of the stopped batteries are shown in Fig. S1†. After dried in the vacuum oven, the anode materials were collected for TEM, Raman and XPS observations.

Results and discussion

Composition and structure characterization

Fig. 1(a) is a scanning electron microscope (SEM) image of $FeMoO_4$ nanorods synthesized by the one-step solvothermal method. The nanorods have a length in the range of 300-500 nm and a diameter of 50-100 nm. The energy dispersive spectroscopic (EDS) measurements in Fig. S2† reveals that the nanorods are composed of Fe, Mo, and O in a ratio of about 1:1:6. Fig. 1(b) depicts a typical X-ray diffraction (XRD) pattern of the as-prepared nanorods, which matches well with the standard diffractions of monoclinic β-$FeMoO_4$ (JCPDS # 22-0628); and two relatively weaker diffraction peaks at 28.2 ° and 40.9 ° (denoted with stars) are also detected, which can be assigned to -220 and -223 planes of α-$FeMoO_4$ (JCPDS # 22-1115). The XRD measurement indicates that the sample mainly comprises β-$FeMoO_4$ phase with a small amount of α-$FeMoO_4$ impurity. TEM observations in Fig. 1(c) and its inset verify that the $FeMoO_4$ nanorods are mesoporous with pore size of ~10 nm in diameter. The nitrogen adsorption-desorption test further revealed a specific surface area of 84.2 $m^2 g^{-1}$, and a pore size distribution around 10 nm by using the BJH method (Fig. S3†), which is in consistence with the TEM observations. Fig. 1(d) is the high-resolution TEM (HRTEM) image obtained on the same nanorod. The marked lattice fringes with d-spacing of

0.34 and 0.33 nm agree well with the -220 and -202 planes of β-FeMoO$_4$ crystal. The corresponding electron diffraction pattern taken along the zone axis of [111] suggests the single crystal nature of the nanorod.

By stopping the solvothermal reaction after different durations, we studied the growth process of the FeMoO$_4$ nanorods. As suggested by the XRD patterns (Fig. S4†), during the whole growth procedure, both α and β phase of FeMoO$_4$ existing in the samples. However, the content of β phase increased gradually with the reaction time, and the majority of the sample after reaction for 24 hours is in β phase.[13] In the SEM and TEM observations (Fig. S5†), it was revealed that FeMoO$_4$ nanoparticles of 50-100 nm in size were formed after 1 h, and the nanoparticles were developed to nanorods as the reaction time was extended to 4 h. At this stage, the nanorods had a rough surface with some nanoparticles attached. These nanoparticles were suggested to be the precursors for the formation of FeMoO$_4$ nanorods,[25] and they aggregated at the end of nanorods growing along the [121] direction. Nanorods with a smooth surface and porous interior were observed as the reaction was prolonged to 12 hours, further extending the reaction time did not give significant change in the dimension, morphology, and porous structure of nanorods.

XPS was also carried out to study the chemical composition of nanorods. The survey spectrum in Fig. S6† confirms that the sample contains Fe, Mo, and O, and the atomic ratio of Fe/Mo is about 1:1. The high-resolution Fe 2p and Mo 3d XPS spectra are presented in Fig. 1(e) and 1(f), respectively. The peaks at 710.5 and 724.1 eV for Fe 2p$_{3/2}$ and Fe 2p$_{1/2}$ indicate the Fe^{2+} oxidation state; and Mo 3d peaks at the binding energies of 232.3 and 235.5 eV suggest the Mo^{6+} oxidation state.[25] The deconvolution of the O 1s peaks, as shown in Fig. S7†, reveals two components at 530.4 and 531.9 eV, which are assigned to the lattice oxygen and chemisorbed oxygen, respectively. The XPS results confirm the formation of FeMoO$_4$, which is consistent with the EDS and XRD results.[11]

Electrochemical performances

The cycling performance of $FeMoO_4$ nanorods as the anode of a LIB was tested by galvanostatic charge-discharge measurement at a rate of 1C. As shown in Fig. 2(a), despite of a high initial discharge capacity, the capacity faded tremendously from 1134 (2nd cycle) to 451 mAh g^{-1} (50th cycle). The drastic capacity decrease in this period was ascribed to the continuous and irreversible consumption of electrode materials for the formation of an solid electrolyte interface (SEI) layer.[24] Then the capacity started to increase gradually till an utmost value of 1265 mAh g^{-1} was reached at about 500th cycle. Noticeably, the capacity is over 300 % larger than the theoretical capacity of traditional graphite anode (~370 mAh g^{-1}), and it is also higher than the theoretical capacity of $FeMoO_4$ (992.3 mAh g^{-1}). After that, the capacity reduced again at a relatively low rate but still maintained higher than 1110 mAh g^{-1} till 1000th cycle. Correspondingly, the Coulombic efficiency increased form 70 % of the first cycle to above 99 % after the 50th cycle, which could be considered as an indication of the formation of a stable SEI layer after 50 cycles.[26]

As suggested by the long-term cycling performance, the critical capacitance points at 50th, 500th, and 1000th cycles in the battery life were selected for further investigation. We tested the rate capabilities of $FeMoO_4$ nanorod anode by using stepped rates of 1C, 2C, 5C, 10C, 1C, and 0.1C at different stages around 50th, 500th, and 1000th cycles (termed as stages I, II, and III, respectively), as depicted in Fig. 2(b) and (c). The 1C capacitance exhibited the similar trend as that in Fig. 2(a), and the rate performance of the electrode showed the same characteristics at these stages, i.e., the capacities decreased as the current density increased from 1C to 10C, and they recovered to almost their original values as the current density was switched back to 1C. Further decreasing the current density to 0.1C led to even higher capacities. However, close observation of the enlarged views in Fig. 2(c) revealed slight difference for the rate performances at different stages. When the current density decreased

from 10C to 1C or from 0.1C to 1C, the capacity in stage II and III could recover more rapidly to its initial capacity values as compared with those in stages I. It is known that the rate capability depends strongly on both electron and ion conductivities of the electrode,[27] the improved rate capability in stage II and III should be due to the structural evolution of $FeMoO_4$ nanorods as discussed below.

Cyclic voltammetry (CV) and electrochemical impedance spectroscopy (EIS) measurements of the batteries at the corresponding stages were also performed. Fig. 2(d) displays the CV curves obtained for the 1st, 2nd, 3rd, 50th, 500th, and 1000th cycles of galvanostatic charge-discharge process. For the cathodic curves, several peaks were observed: i) the peak around 0.1 V in the first discharge was attributed to the irreversible formation of SEI layer,[8] and it gradually disappeared after 50 cycles; ii) The broad peak between 1.5 and 2.0 in the first discharge were assigned to the irreversible intercalation of lithium ions into the crystal lattice, which also disappeared in the following cycles;[28] iii) Starting with the 2nd cycle, the peak around 0.7 V was due to the reduction of Fe^{2+} or Fe^{3+} to Fe^0.[16,19] which maintains its intensity till the 50th cycle, and it could still be distinguished after 500 cycles; iv) The peaks in the ranges of 0.2-0.4 V and 1.2-1.4 V were associated with the multi-step reduction from Mo^{6+} to Mo^0, which are also evident in the 50th and 500th cycles.[28,29] Correspondingly, in the anodic curves, two broad peaks around 1.5 and 1.8 V ascribed to the oxidation of Fe and Mo metals were observed in the first cycle, and they merged to a broad peak around 1.5 V after 50 cycles. In the 500th and 1000th cycles, the peak gradually shifted to a lower potential of ~1.4 V, implying the alleviating polarization after the 50th cycle.[30] Since the integrated peak area was equal to the capacity, [31] the current intensity of the CV curve at 500th cycle is the highest, agreeing with the cycling performance in Fig. 2(a).

Fig. 2(e) presents the EIS interceptions of the freshly fabricated cell, and the cells after testing for 1, 50, 500, and 1000 galvanostatic charge-discharge cycles at a rate of 1C. All the

Nyquist plots exhibited a semicircle in the high frequency region followed by a straight line in the low frequency region, being related to the interface charge transfer process and diffusion process, respectively. It is apparent that the charge transfer resistance (R_{ct}) persistently decreased till 500th cycle, i.e., from ~438 Ω for a freshly fabricated cell to ~23 Ω at 500th cycle, and then increased slightly to ~54 Ω at 1000th cycle (The fitting results and equivalent circuits are shown in Table S1†). The decreasing R_{ct} in the 500 cycles indicates the activation of electrodes and improved kinetics of the reaction.[32] In addition, the fitted surface film resistance (R_f) and Warburg impedance (Z_w) shows a generally decreasing trend as cycling, except for the abnormally increased 50th cycle. It suggests that the diffusion resistance of lithium ions increased around the 50th cycle due to the formation of thick and unstable SEI layers over the nanorods.[33,34] After that, as discussed below, the polycrystalline nanorods were gradually changed to amorphous state with refined grains and finally converted to nanosheets, and thinner and stable SEI layers were grown on the nanosheets surfaces, which was beneficial for the lithium insertion/extraction and electron transfer processes.[24, 34] The EIS measurements are in accordance with the alleviated polarization effect at 50th cycle (from CV curves) and improved rating performance after 50th cycle.

Structural and chemical evolutions

The morphological transformation of the electrode materials was systematically investigated at each critical stage of the charge/discharge process. Fig. 3 is a set of TEM images showing the morphology evolution of FeMoO$_4$ nanorods at different stages of cycling (1st, 50th, 500th, and 1000th cycles) at a rate of 1C. After one cycle, the FeMoO$_4$ nanorods had no obvious change (Fig. 3(a)). However, the enlarged view in the inset in Fig. 3(a) revealed increased porosity of nanorods. The HRTEM image and the corresponding fast Fourier transform (FFT) pattern in Fig. 3(b) further showed reduced crystallinity after the first lithium ion intercalation. After 50 cycles, the nanorods presented a rough surface composing of large

amount of nanoparticles and enlarged pore size/space, as shown in Fig. 3(c). The transformation of nanorods to polycrystalline structure is apparently evidenced in HRTEM and corresponding FFT pattern in Fig. 3(d). The fragmentation of the nanorods surface and continuous formation of SEI layer are responsible for the drastic specific capacitance fading during the period of the first 50 cycles. Moreover, the SEI layer at this stage is thick and unstable (also suggested by ref. 23), resulting in an increased ion diffusion resistance, serious polarization and bad rating performance. Fortunately, after the initial 50 cycles, a stable SEI layer was formed as indicated by the stabilized Coulombic efficiency, which led to the recovery of electrochemical performance of the battery.

From 50th to ~500th cycle, the nanorods were gradually transformed to nanosteets with further grain refinement, bringing about large quantities of pores and larger surface area as suggested by Fig. 3(e). High-density backbones could still be distinguished in the center of nanosheets which comprised amorphous materials and small crystals, as observed in Fig. 3(f) and corresponding FFT pattern inserted. The formation of nanosheets could be more clearly observed in the SEM images in Fig. S8†. Accordingly, such a structural transformation resulted in gradual capacity increase in the following 500 cycles, together with the enhanced rating performance, alleviated polarization, and largely reduced charge transfer and diffusion resistances. Impressively, for the 1000th cycle, nanorods have been completely converted to nanosheets with an average size of several hundreds of nanometer (Fig. 3(g) and Fig. S8†). As indicated by the FFT pattern and HRTEM image (Fig. 3(h)), the layer is in amorphous state with nanocrystals of ~5 nm in size embedded. These porous and amorphous layers with larger specific surface area as compared with the original nanorod are believed to provide increased Li^{+} active sites and enable improved reaction kinetics. Furthermore, the distributions of O, Fe and Mo elements were studied by using high-angle annular dark-field scanning transmission electron microscope (HAADF-STEM) and EDS elemental mapping at 1st, 50th, 500th and

1000th cycles (Fig. S9†). It was demonstrated that these elements were distributed uniformly over the nanorods at different stages. As a result, the capacity maintained stable against the repeated charge-discharge cycling and had enhanced rate capability. As illustrated by the schematic diagram in Fig. 3(i), the original $FeMoO_4$ nanorods experienced structural transformation from single crystals to polycrystalline state with refined grains, and finally converted to amorphous nanosheets. The morphology evolution was driven by the electrochemical reactions and continuously expanding and contracting of the metal oxide species in the discharge and charge process, which are closely related to the electrochemical performance of the electrode at different stages.

For the purpose of identifying the chemical reactions during the charge and discharge process, the electrode materials after different cycles were investigated by Raman and XPS. Fig. 4(a) displays the Raman spectra of the as-prepared $FeMoO_4$ nanorods and those after charge/discharge for 1, 50, 500, and 1000 cycles. For the pristine nanorods, the peaks at 823, 879 and 926 cm^{-1} (as marked by diamond) are assigned to $FeMoO_4$.[10] In the subsequent cycles, a few new peaks are observed. For instance, peaks at 225, 293 and 416 cm^{-1} are assigned to Fe_2O_3 (as marked by club);[35] the broad peak at 1330 cm^{-1} may come from conductive agent carbon (~1350 cm^{-1} as marked by spade) in the electrode two-magnon scattering of Fe_2O_3 (~1320 cm^{-1}); and the peaks at 369, 660, 811 and 987 cm^{-1} are attributed to MoO_3 (marked with heart).[36] These peaks with considerable relative intensities could still be revealed till 50th cycle, implying the existence of Fe_2O_3 and MoO_3 phases during the first 50 cycles. However, the peaks disappeared in the spectra for the 500th and 1000th cycles, leaving only the carbon signal at 1350 cm^{-1}. XRD measurements of the samples were also performed after the charge and discharge processes, as depicted in Fig. S10†. The results agree with those drawn from Raman and TEM characterization very well: (1) the original $FeMoO_4$ transformed to Fe_2O_3

and MoO_3 after the first cycle, and (2) the crystallinity of the electrode materials degraded along with cycles and finally turned to amorphous.

Fig. 4(b) depicts high-resolution Fe 2p XPS spectra collected from the pristine $FeMoO_4$ nanorods and electrode materials after 1 cycle and 1000 cycles. After the 1st cycle, both Fe $2p_{3/2}$ (710.5 eV) and Fe $2p_{1/2}$ (724.1 eV) were shifted to higher binding energy, i.e., Fe $2p_{3/2}$ (711.1 eV) and Fe $2p_{1/2}$ (724.8 eV), respectively, implying that Fe^{2+} was changed to Fe^{3+} oxidation state after the first discharge-charge cycle.[37,38] In contrast, the valence of Mo element maintains the same during the 1000 discharge-charge cycles, as suggested by the high-resolution Mo 3d XPS spectrum in Fig. S11†.

In the first discharge, the crystal structure of $FeMoO_4$ was destructed followed by the formation of metal nanoparticles in amorphous matrix of Li_2O, as described by equation (1).

$$FeMoO_4 + 8Li^+ + 8e^- \rightarrow Fe + Mo + 4Li_2O \tag{1}$$

According to the Raman and XPS results, this process is irreversible since binary metal oxides are detected in the following cycles. In the subsequent cycles, transformation between Fe, Mo metal particles and their respective metal oxides occurs reversibly, as shown by equation (2) and (3).

$$2Fe + 3Li_2O \leftrightarrow Fe_2O_3 + 6Li^+ + 6e^- \tag{2}$$

$$Mo + 3Li_2O \leftrightarrow MoO_3 + 6Li^+ + 6e^- \tag{3}$$

The theoretical capacity for $FeMoO_4$ including the reduction of Mo^{6+} to Mo^0 and Fe^{2+} to Fe^0 by the lithium ions is calculated to be 992.25 mAh g^{-1}. After the reactivation process, the stabilized capacity reached up to 1265 mAh g^{-1} at about 500th cycle, which is 25% higher than the theoretical capacity of $FeMoO_4$. The oxidization of Fe^{2+} to Fe^{3+} should account for the even higher specific capacity as compared with the theoretical one. As a reference, the theoretical capacity of Fe_2O_3 (1117 mAh g^{-1}) is higher than that of FeO (744 mAh g^{-1}).[34,39]

For the electrodes based on C, Si, and Sn, grain refinement (pulverization) and amorphization lead to degradation of electrode with reduced capacity and poor cycling stability. However, for the MO electrodes including TMOs, the grain refinement and amorphization may play positive roles affecting the electrochemical performance of electrodes. 1) Previous research have suggested that amorphization of MO crystals leads to narrowed potential hysteresis and faster conversion reaction rates, thus more reversible electrochemical reaction than that of crystalline phase could be achieved.[31,40] Similarly, the transformation to amorphous structure containing nanocrystals in our case should be beneficial for preventing the agglomeration of metal grains and improving the electrochemical reaction kinetics, resulting in much better cycling and rating performance than the initial crystal $FeMoO_4$ nanorods. 2) The increased lateral size of nanostructures, enhanced open-boundaries and effective interfacial area are significant for maintaining the high capacities.[41] The increased lateral size of nanostructures, enhanced open-boundaries and effective interfacial area are vital for maintaining the high capacities. Due to the structural transformation of nanorods to amorphous layers, it is proposed that lithium ions and electrons are separately stored at the interfacial regions where lithium ions are collected at phase boundaries, according to the suggested interfacial charging mechanism.[42-44] Extra lithium ions could be accommodated in the interfacial space between the amorphous layers, leading to an improved reversible capacity, which became predominant along with cycling.

Conclusion

$FeMoO_4$ nanorods have been demonstrated as a high-performance anode material for LIBs, which exhibits superior cycling and rating performance as compared with conventional graphitic electrode. Through elaborately investigated on the structural and chemical evolution process of the electrode materials by comprehensive characterizations, a self-induced structural optimization (e.g., grain refinement with increased porosity and structure

transformation from crystalline nanorods to amorphous nanosheets) has been exposed. Significantly, combining the development of electrochemical performance as cycles and structural and chemical evolution, we conclude that the structural transformation and amorphization of TMO electrode material improve the electrochemical reaction kinetics and increases valid surface areas, contributing to the capacity fading, recovery and stabilization, which differs from the cases of electrodes based on elemental materials such as C, Si and Sn. The combining investigation between the observations and electrochemical analysis in this work may give a deeper understanding about the electrochemical reaction mechanism of the TMOs for the LIB anodes.

Acknowledgements

References

1 G. G. Guo, H. B. Wu and X. W. Lou, *Adv. Energy Mater.*, 2014, **4**, 1400422.

2 L. Hu, H. Zhong, X. R. Zheng, Y. M. Huang, P. Zhang and Q. W. Chen, *Sci. Rep.*, 2012, **2**, 986.

3 W. P. Kang, Y. B. Tang, W. Y. Li, X. Yang, H. T.Xue, Q. D. Yang and C. S. Lee, *Nanoscale*, 2015, **7**, 225-231.

4 F. Wang, R. Robert, N. A. Chernova, N. Pereira, F. Omenya, F. Badway, X. Hua, M. Ruotolo, R. G. Zhang, L. J. Wu, V. Volkov, D. Su, B. Key, M. S. Whittingham, C. P. Grey, G. G. Amatucci, Y. M. Zhu and J. Graetz, *J. Am. Chem. Soc.*, 2011, **133**, 18828-18836.

5 N. N. Leyzerovich, K. G. Bramnik, T. Buhrmester, H. Ehrenberg and H. Fuess, *J. Power Sources*, 2004, **127**, 76-84.

6 S. S. Kim, S. Ogura, H. Ikuta, Y. Uchimoto and M. Wakihara, *Solid State Ionics*, 2002, **146**, 249-256.

7 W. Xiao, J. S. Chen, C. M. Li, R. Xu and X. W. Lou, *Chem. Mater.*, 2010, **22**, 746-754.

8 C. T. Cherian, M. V. Reddy, S. C. Haur and B. V. R. Chowdari, *ACS Appl. Mater. Interfaces*, 2013, **5**, 918-923.

9 R. N. Singh, J. P. Singh and A. Singh, *Int. J. Hydrogen Energy*, 2008, **33**, 4260-4264.

10 Y. H. Wang, P. He, W. Lei, F. Q. Dong and T. H. Zhang, *Compos. Sci. Technol.*, 2014, **103**, 16-21.

11 B. Senthilkumar and R. K. Selvan, *J. Colloid Interface Sci.*, 2014, **426**, 280-286.

12 J. L. Brito and A. L. Barbosa, *J. Catal.*, 1997, **171**, 467-475.

13 Z. C. Ju, E. Zhang, Y. L. Zhao, Z. Xing, Q. C. Zhuang, Y. H. Qiang and Y. T. Qian, *Small*, 2015, 10.1002/smll.201501294.

14 F. Lin, D. Nordlund, T. C. Weng, Y. Zhu, C. M. Ban, R. M. Richards and H. L. Xin, *Nat. Commun.*, 2014, **5**, 3358.

15 Y. G. Zhu, Y. Wang, Y. M. Shi, Z. X. Huang, L. Fu and H. Y. Yang, *Adv. Energy Mater.*, 2014, **4**, 1301788.

16 X. Gu, L. Chen, Z. C. Ju, H. Y. Xu, J. Yang and Y. T. Qian, *Adv. Funct. Mater.*, 2013, **23**, 4049-4056.

17 D. N. Wang, J. L. Yang, X. F. Li, D. S. Geng, R. Y. Li, M. Cai, T. K. Sham and X. L. Sun, *Energy Environ. Sci.*, 2013, **6**, 2900-2906.

18 J. S. Luo, J. L. Liu, Z. Y. Zeng, C. F. Ng, L. J. Ma, H. Zhang, J. Y. Lin, Z. X. Shen and H. J. Fan, *Nano Lett.*, 2013, **13**, 6136-6143.

19 X. Y. Li, Y. Y. Ma, L. Qin, Z. Y. Zhang, Z. Zhang, Y. Z. Zheng and Y. Q. Qu, *J. Mater. Chem. A*, 2015, **3**, 2158-2165.

20 Y. M. Sun, X. L. Hu, W. Luo and Y. H. Huang, *ACS nano*, 2011, **5**, 7100-7107.

21 W. Wei, S. B. Yang, H. X. Zhou, I. Lieberwirth, X. L. Feng and K. Müllen, *Adv. Mater.*, 2013, **25**, 2909-2914.

22 Z. Y. Cai, L. Xu, M. Y. Yan, C. H. Han, L. He, K. M. Hercule, C. J. Niu, Z. F. Yuan, W. W. Xu, L. B. Qu, K. N. Zhao and L. Q. Mai, *NanoLett.*, 2015, **15**, 738-744.

23 Y. F. Liu, J. M. Xu, X. Y. Qin, H. X. Xin, X. Q. Yuan, J. Zhang, D. Li and C. J. Song, *J. Mater. Chem. A,* 2015, **3**, 9682-9688.

24 H. T. Sun, G. Q. Xin, T. Hu, M. P. Yu, D. L. Shao, X. Sun and J. Lian, *Nat. Commun.*, 2014, **5**, 4526.

25 Z. Y. Zhang, C. G. Hua, M. Hashima, P. Chenb, Y. Q. Xiong and C. L. Zhang, *Mater. Sci. Eng. B,* 2011, **176**, 756-761.

26 W. M. Zhang, X. L. Wu, J. S. Hu, Y. G.Guo and L. J. Wan, *Adv. Funct. Mater.*, 2008, **18**, 3941-3946.

27 M. M. Kalantarian, S. Asgari and P. Mustarelli, *J. Mater. Chem. A*, 2014, **2**, 107-115.

28 P. J. Lu, M. Lei and J. Liu, *CrystEngComm,* 2014, **16**, 6745-6755.

29 X. Li, J. T. Xu, L. Mei, Z. J. Zhang, C. Y. Cui, H. K. Liu, J. M. Ma and S. X. Dou, *J. Mater. Chem. A*, 2015, **3**, 3257-3260.

30 T. Subburaj, K. Prasanna, K. J. Kim, P. R. Ilango, Y. N. Jo and C. W. Lee, *J. Power Sources,* 2015, **280**, 23-29.

31 J. C. Guo, Q. Liu, C. S. Wang and M. R. Zachariah, *Adv. Funct. Mater.*, 2012, **22**, 803-811.

32 Y. R. Zhong, M. Yang, X. L. Zhou, Y. T. Luo, J. P. Wei and Z. Zhou, *Adv. Mater.*, 2015, **27**, 806-812.

33 G. M. Zhou, D. W. Wang, L. C. Yin, N. Li, F. Li and H. M. Cheng, *ACS nano*, 2012, **6**, 3214-3223.

34 Y. Ma, C. Zhang, G. Ji and J. Y. Lee, *J. Mater. Chem.*, 2012, **22**, 7845-7850.

35 M. V. Reddy, T. Yu, C. H. Sow, Z. X. Shen, C. T. Lim, G. V. S. Rao and B. V. R. Chowdari, *Adv. Funct. Mater.*, 2007, **17**, 2792-2799.

36 B. C. Windom, W. G. Sawyer and D. W. Hahn, *TribolLett.*, 2011, **42**, 301-319.

37 T. Yamashita and P. Hayes, *Appl. Surf. Sci.*, 2008, **254**, 2441-2449.

38 Z. Y. Zhang, W. Y. Li, R. J. Zou, W. P. Kang, Y. S. Chui, M. F. Yuen, C. S. Lee and W. J. Zhang, *J. Mater. Chem. A*, 2015, **3**, 6990-6997.

39 Y. M. Sun, X. L. Hu, W. Luo, F. F. Xia and Y. H. Huang, *Adv. Funct. Mater.*, 2013, **23**, 2436-2444.

40 O. Delmer, P. Balaya, L. Kienle and J. Maier, *Adv. Mater.*, 2008, **20**, 501-505.

41 S. B. Yang, Y. Sun, L. Chen, Y. Hernandez, X. L. Feng and K. Müllen, *Sci. Rep.*, 2012, **2**, 427.

42 Q. Wang, J. Sun, Q. Wang, D. A. Zhang, L. L. Xing and X. Y. Xue, *J. Mater. Chem. A*, 2015, 3, 5083-5091.

43 W. Wang, D. A. Zhang, W. Wang, J. Sun, L. L. Xing and X. Y. Xue, *Electrochim. Acta*, 2014, 146, 411-418.
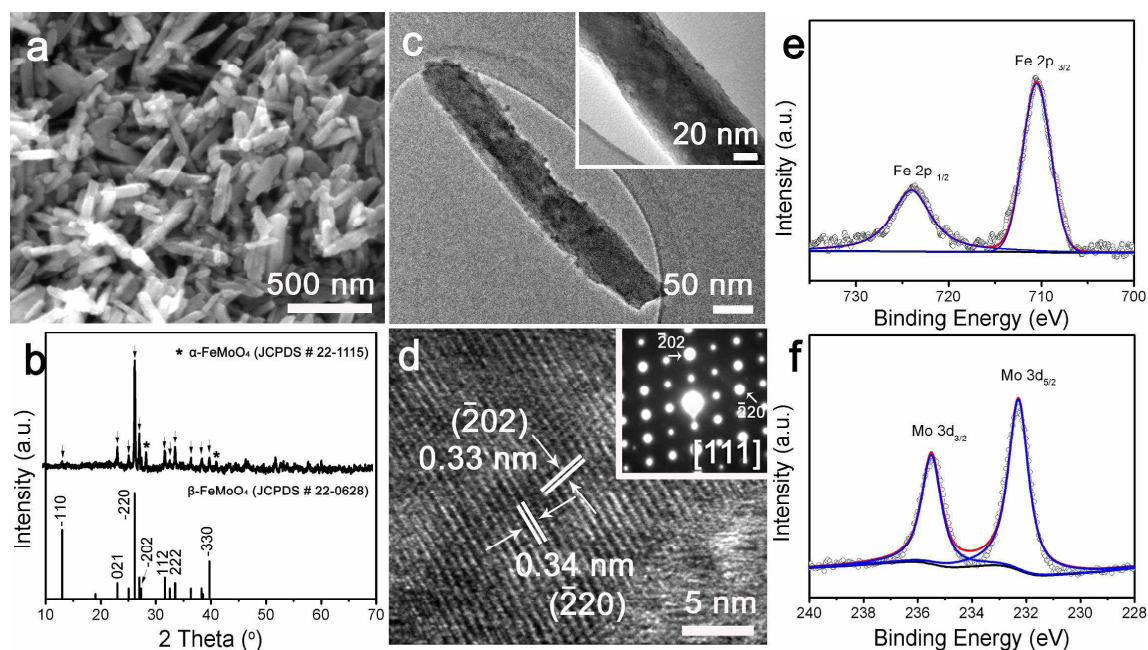
44 J. Maier, *Faraday Discuss.,* 2007, 134, 51-66.

Fig. 1. (a) SEM image and of the FeMoO$_4$ nanorods. (b) XRD pattern of the sample in reference to the standard diffractions of β-FeMoO$_4$. (c) TEM image of an individual FeMoO$_4$ nanorod and the inset is the enlarged image. (d) HRTEM image of a nanorod with marked lattice fringes. The inset is the electron diffraction pattern of the nanorod. (e) The high-resolution XPS Fe 2p spectrum and (f) Mo 3d spectrum of the sample.
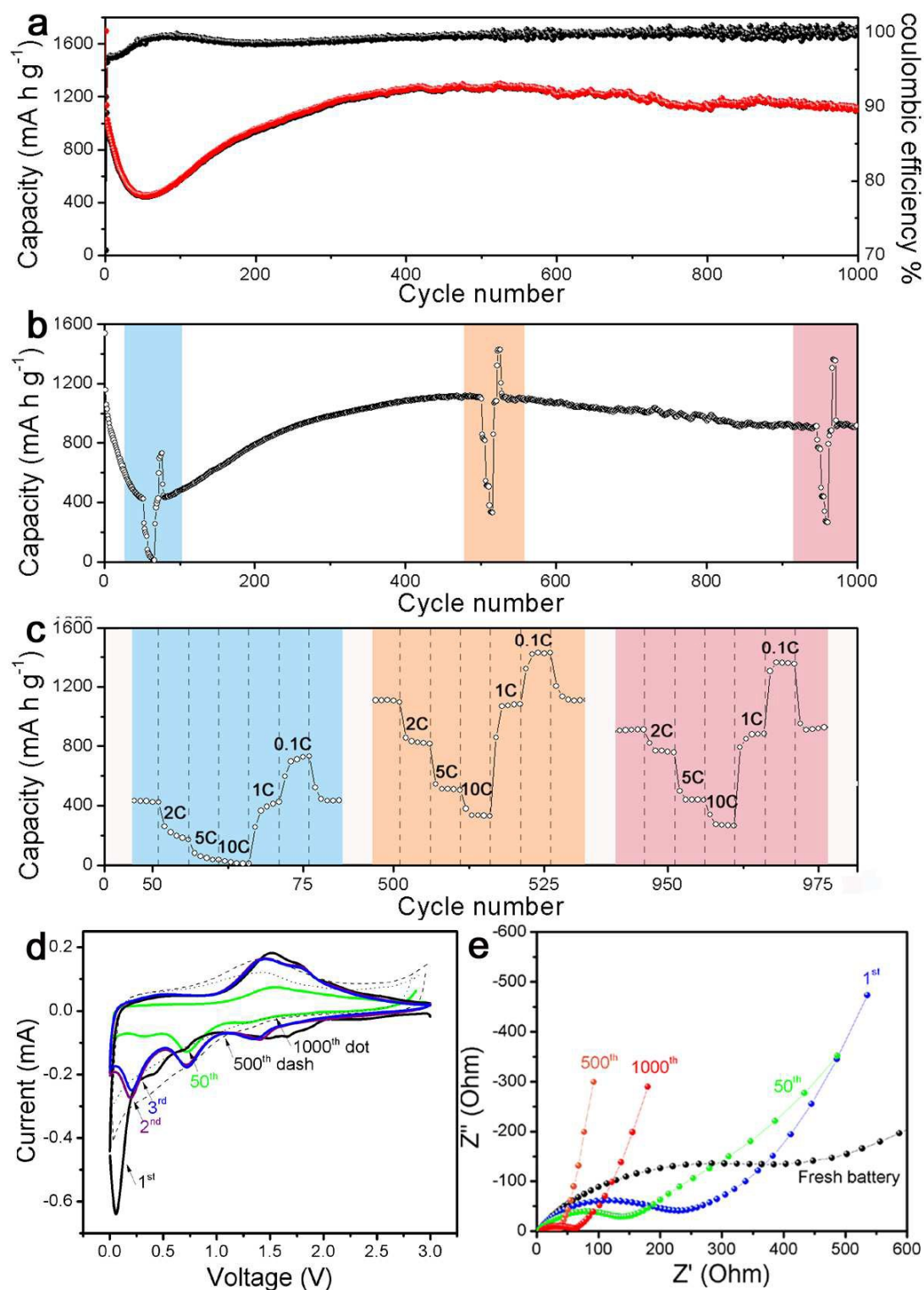
Fig. 2. (a) Cycling performance and coulombic efficiency of the FeMoO$_4$ nanorods anode at a rate of 1C in 1000 cycles. (b) Rate capability test of FeMoO$_4$ nanorods anode at the rates of 1C, 2C, 5C, 1C, 10C, and 0.1C and at different stage (stage I, II, III correspond to that around

50th, 500th, 1000th cycle, respectively) of cycling, respectively. (c) Enlarged plot areas of the

cycle stages I, II and III for clearer observation. (d) CV curves obtained on the cells of the

first three cycles, and after 50, 500, and 1000 cycles at galvanostatic charge-discharge. (e) EIS

spectra of the freshly fabricated cell, and the cells experienced for 1, 50, 500, and 1000

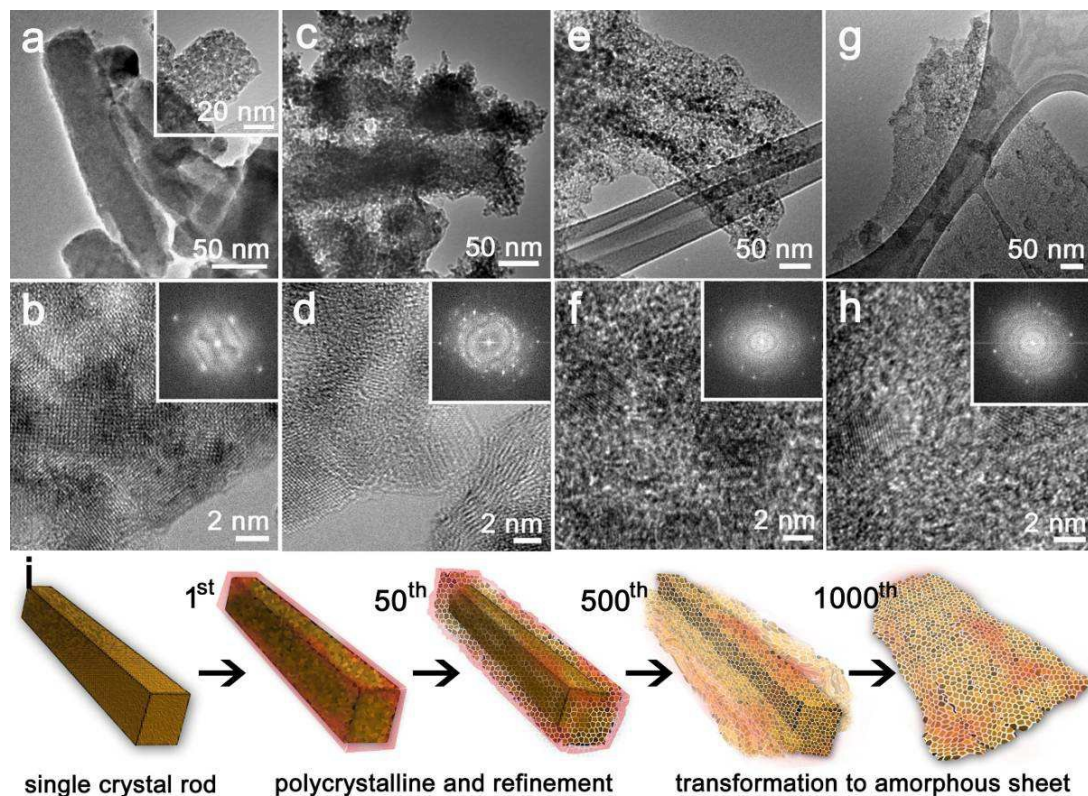galvanostatic charge-discharge cycles with a rate of 1C.

Fig. 3. TEM and corresponding HRTEM images of the $FeMoO_4$ nanorods electrode material

after various battery cycles (a, b) 1, (c, d) 50, (e, f) 500, (g, h) 1000, insets are their FFT

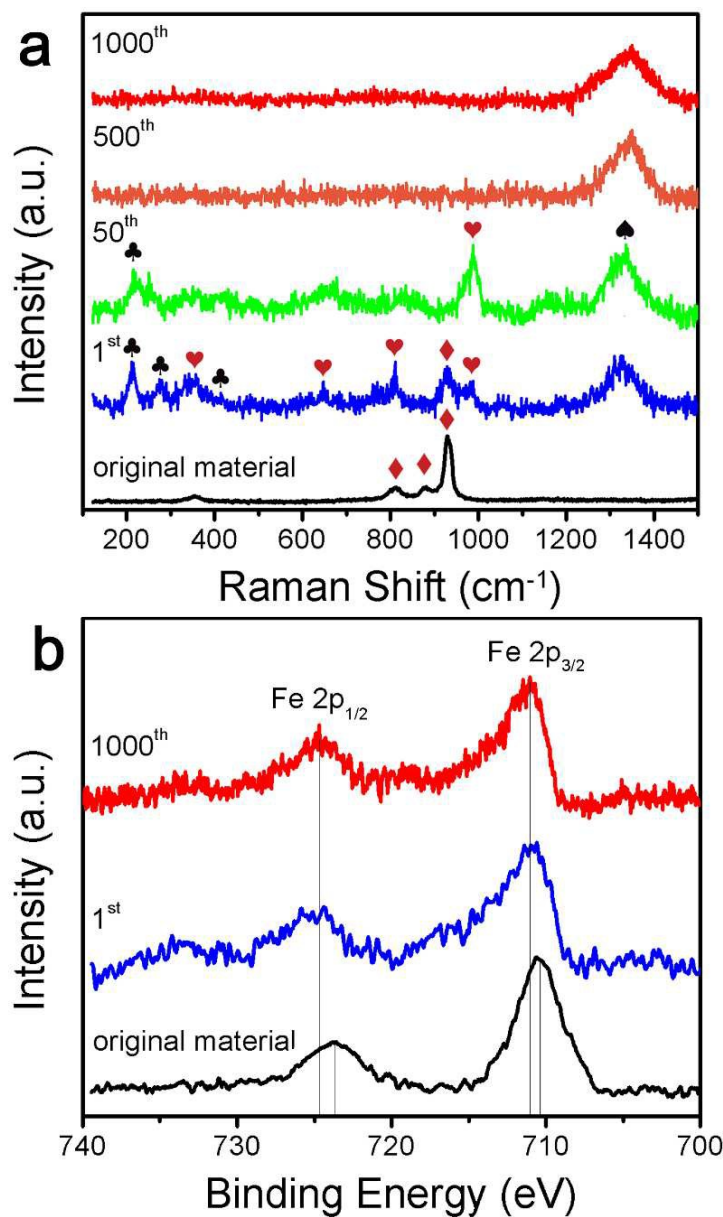patterns. (i) Schematic diagram of the morphology evolution of $FeMoO_4$ nanorods with cycles.

Fig. 4. (a) Raman spectra of the original $FeMoO_4$ nanorods and the electrode material after different cycles (1, 50, 500 and 1000). (b) The high-resolution Fe 2p XPS spectrum of the original $FeMoO_4$ nanorods, after the 1st cycle and 1000th cycle.

FeMoO₄ nanorods are demonstrated as high-performance anode of LIBs which exhibits enhanced cycling and rating performance, improved charge transfer and ion diffusion conductivity as long-term cycling. The structural and chemical evolution of the nanorods during a long-term cycling is systematically exposed. The improved battery performance is attributed to the self-induced structural optimization.

Key word

Iron molybdate, lithium ion battery anode, structural evolution, phase transformation

Zhenyu Zhang, Wenyue Li, Tsz-Wai Ng, Wenpei Kang, Chun-Sing Lee, and Wenjun Zhang*

Iron (II) molybdate (FeMoO₄) nanorods as high-performance anode of lithium ion battery: structural and chemical evolutions upon cycling

ToC figure

single crystal nanorod   polycrystal nanorod   grain refinement   transformation to amorphous nanosheets